Magnesium Pincer Complexes for Pyridine Hydrogenation

Main-Metal Catalysis

4052LEON4: Bachelor Final Project

Robert Sylvia

Delft University of Technology

TU Delft

Magnesium Pincer Complexes for Pyridine Hydrogenation

Main-Metal Catalysis

by

Robert Sylvia

Professor:	Dr. Evgeny Pidko
Main Supervisor:	Dr. Evgeny Pidko
Technical Supervisors:	Adarsh Kalikadien, Dr. Aleksandr Kolganov, Margareth Baidun
Project Duration:	April, 2025 - July, 2025
Faculty:	Chemical Engineering, Applied Sciences
Research Group:	Inorganic Systems Engineering

Cover:	Free Chimney Smoke Image by rawpixel under CC0 (Cropped)
Style:	TU Delft Report Style, with modifications by Daan Zwaneveld

TU Delft

Contents

1

Introduction

The development of a diverse array of energy sources is a societal necessity to address growing energy demand without furthering fossil fuel depletion and environmental destruction.[1,2] Hydrogen is one of the most promising energy sources for meeting sustainability goals, however advanced realization has been limited by the challenges of its storage and transport.[3] The development of highly efficient storage technologies is therefore imperative to overcome this bottleneck.[2] Physical storage solutions for hydrogen are riddled with drawbacks, such as volumetric constraints and costly liquefaction. In contrast, chemical storage solutions, especially using organic hydrogen carriers, have emerged as a promising alternative.

Chemical storage of hydrogen using organic hydrogen carriers has been found advantageous from environmental, economic, and technical viewpoints, and is, perhaps consequently, a rather mature technology within the sector.[2,3] Environmentally, organic hydrogen carriers can constitute a closed carbon system, thereby reducing pollution.[3] Economically, organic hydrogen carriers are favorable because they are compatible with existing fossil fuel infrastructure, meaning that large capital investments are not necessary. Technically, they are considered safe to handle, and the hydrogenation processes used are well-understood, with highly optimized catalysts.[2] However, in spite of the aforementioned advantages, storage in organic carriers has yet to be commercialized on a large scale.[2]

The simplest candidates for organic hydrogen carriers are cyclic hydrocarbons.[3] Cyclic hydrocarbons satisfy the desire for a closed carbon cycle, as no CO_x molecules are produced, and also offer a desirable gravimetric capacity of hydrogen. Unfortunately, the dehydrogenation process requires high temperatures (around 150-350 $^\circ C$) due to the strongly endothermic nature of the dehydrogenation reaction, which is problematic for homogeneous catalysis and mobile applications.[2,3] Recent studies have found that substituting nitrogen atoms into the hydrocarbon skeleton is a more thermodynamically viable option for homogeneous catalysis, as this lowers the endothermicity of the dehydrogenation process.[1–3] However, compared to unsubstituted cyclohexanes, adding nitrogen introduces some disadvantages, such as lower gravimetric density, possibility of solid products, and most notably the risk of undesired side reactions occurring.[2] These side reactions have been reported as minimizable via steric effects of ligands on the N-heteroatom.

Ligand design can greatly aid in controlling the reactivity of complexes used in homogeneous catalysis, including the catalytic pathways of hydrogenation reactions.[2,4] Pincer ligands, tridentate ligands that coordinate to adjacent binding sites on a metal complex, have become particularly popular thanks to their versatility and the robustness of the formed complexes.[4] Notably, hemilability, the ability of a donor group to reversibly dissociate and thereby open up a coordination site, is often seen in pincer ligands, and can be important for catalytic efficiency.[4] As such, there are numerous examples in literature of catalyzing the hydrogenation and dehydrogenation reactions using pincer ligands: Milstein et al. used ruthenium-based PNN pincer ligands for hydrogenation and dehydrogenation reactions in hydrogen storage[3]; Wang et al. used iridium-based PCP complexes as a homogeneous catalyst for various dehydrogenation reactions[1]; Sánchez et al. reported effective ruthenium-based CNN pincer ligands

for hydrogenation and dehydrogenation of N-heterocycles.[5] While pincer ligands are a powerful tool for directing the reactivity and properties of complexes, they are not the only lever available.

The choice of metal also significantly alters the activity and dynamics of complexes, granting further control and variation.[2] Historically, the vast majority of metals used for catalysis have been noble metals, including the three aforementioned examples, but in recent years there have been significant developments in first-row transition-metal complexes.[6,7] Especially noble metals, but also transition metals as a whole, are plagued by low abundance and therefore high cost, in addition to toxicity issues.[6,8] To circumvent these issues, there has been growing interest in main-group metals for catalysis, as they are abundant, non-toxic, and preferable from a sustainability perspective.[8] Recent studies have reported a number of successes in catalysis using main-group metals, though compared to transition metals, main-group metal catalysis is still far less mature.[6,8,9] Rauch et al. successfully used zinc-based PNP^{tBu} complexes to catalyze H_2 activation and product release, finding that metal ligand cooperation (MLC) and hemilability of the phosphorous arms of the pincer ligand are essential.[6] Metal ligand cooperation has been proven an indispensible tool to facilitate bond-activation for hydrogenation reactions, with Sharma et al. very recently revealing that MLC using magnesium complexes can cleave the O-H and C-H bonds of Me_3SiCHN_2.[9] Most interestingly for hydrogenation and H_2 storage is the study by Liang et al. reporting that PNP, PNN, and NNN magnesium-based pincer complexes are feasible for catalyzing the semihydrogenation of internal alkynes and the hydrogenation of alkenes, with a magnesium hydride complex forming initially as the active catalyst.[8]

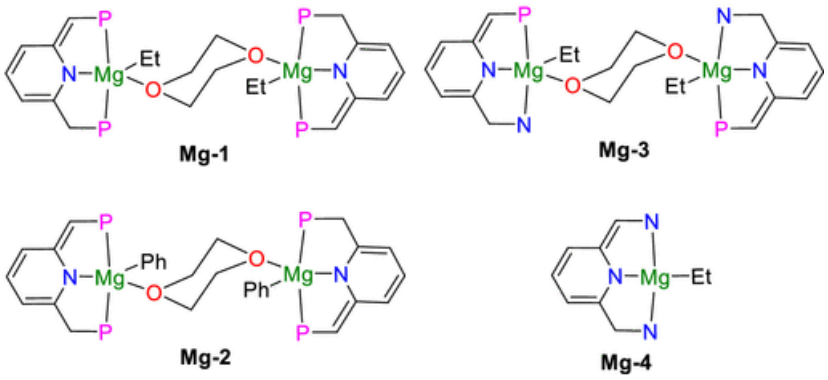

Figure 1.1: Example magnesium pincer complexes synthesized by Liang et al., including PNP, PNN, and NNN pincer ligands[8] (Cropped, Rearranged)

Liang et al. invites further research into the possibilities of these magnesium complexes, stating that they believe it will provide possibilities for the hydrogenation of other compounds as well. What remains to be seen is whether these or similar complexes can be used to catalyze the N-heterocycle hydrogenation processes needed for hydrogen storage.

In this study, an in-silico screening of numerous magnesium-based complexes with coordinated pyridine is conducted to lay groundwork for further study of pyridine hydrogenation and other N-heterocycle hydrogenations using main-metal catalysts. The Gibbs Free Energy of pyridine's coordination is calculated using the 5-coordinated complex as the starting point. Complexes containing carbon monoxide as an auxiliary ligand were found to be thermodynamically unstable, repelling the CO. The Mg-Px bond lengths are additionally obtained as a geometric quantity. The energy of the full dissociation of the ligand and replacement by additional pyridines is also investigated. Hemilability is found for a number of pincer ligands, but is not present in any of the thermodynamically stable complexes. Several suitable candidates for further studies into pyridine hydrogenation are identified based on these quantities.

2

Methodology

2.1. MACE

Since this study investigates 60 different pincer ligands, resulting in a total of 200 unique structures, it was highly prudent to use a high-throughput computational workflow to generate the geometries of the different stereoisomers for each pincer ligand. The software chosen was MACE, which is a fully automated workflow for converting SMILES (Simplified Molecular-Input Line Entry System) of ligands and the metal center into 3D coordinates (.xyz files) of all possible stereochemical configurations.[10] MACE accomplishes this in a number of steps. First, it converts the inputs, which is the metal center, the complex geometry, and the SMILES of the ligands, into all possible configurations in space of the ligands around the central atom. Identical configurations are then removed, as are enantiomers. Once the unique stereoisomers are identified, the 3D coordinates are built using RDKit's distance geometry method. Finally, relaxation is performed using Universal Force Field (UFF). 3D coordinate files (.xyz) are then produced for each unique stereoisomer of each specified complex, which can then be used for higher-level theory geometry optimizations.

2.2. Density Functional Theory

Density Functional Theory (DFT) provides the basis for the higher levels of theory needed for sufficiently accurate geometry optimizations. The following derivations and explanation behind DFT are derived from an earlier unpublished work[11], which is in turn adapted from Cramer's textbook, Essentials of Computational Chemistry.[12] In quantum mechanics, the energy is defined by the eigenvalue returned by the Hamiltonian operator, $\hat{H}$, resulting in the Schrödinger equation in equation (2.1).

$$\hat{H}\Psi = E\Psi \tag{2.1}$$

Unfortunately, solutions to the wave function are high-dimensional and therefore not solvable analytically for systems more complex than a hydrogen atom. For this reason, the Born-Oppenheimer approximation is applied, which uses the fact that electrons move several magnitudes faster than nuclei, allowing for decoupling of electronic and nuclear motion. The electronic relaxation is therefore approximated as instantaneous relative to any given nuclear motion. The nuclear-nuclear repulsive potential becomes constant. These simplifications result in the electronic Schrödinger equation, shown in equation (2.2),

$$(\hat{H}_{\mathsf{el}})\Psi_{\mathsf{el}}(\boldsymbol{q}_{\mathsf{i}}, \boldsymbol{q}_{\mathsf{k}}) = E_{\mathsf{el}}\Psi_{\mathsf{el}}(\boldsymbol{q}_{\mathsf{i}}, \boldsymbol{q}_{\mathsf{k}}) \tag{2.2}$$

where the subscript el indicates usage of the Born-Oppenheimer approximation. Unfortunately, even with the Born-Oppenheimer approximation, there is no analytical solution due to the complexity of the electron-electron interactions. One approach to circumvent this problem is density functional theory, specifically with the Hohenberg-Kohn theorems. The essential point of these theorems is that there is a one-to-one mapping between electron density and the energy of the system, such that for a given

electron density, there is only one possible value for the energy; the energy of the system is a functional of its electron density. This significantly reduces the dimensionality of the problem, as electronic density is a 3-dimensional object (x, y, and z spatial dimensions). To find the electronic density directly at position r_1, one must integrate over all of the wave functions (of all electrons) in all three spatial dimensions. The energy is then decomposed into three terms: the kinetic energy of the electrons T_e, the repulsive potential between electrons V_{ee}, and the attractive potential between electrons and nuclei V_{en} as shown in equation (2.3).

$$E[\rho(\boldsymbol{r})] = T_e[\rho(\boldsymbol{r})] + V_{ee}[\rho(\boldsymbol{r})] + V_{en}[\rho(\boldsymbol{r})] \tag{2.3}$$

The coulombic potentials, terms V_{ee} and V_{en}, are described by the expressions shown in equation (2.4) and equation (2.5), respectively.

$$V_{ee}[\rho(\boldsymbol{r})] = \frac{1}{2}\int\int \frac{\rho(\boldsymbol{r}_1)\rho(\boldsymbol{r}_2)}{|\boldsymbol{r}_1 - \boldsymbol{r}_2|} d\boldsymbol{r}_1 d\boldsymbol{r}_2 \tag{2.4}$$

$$V_{en}[\rho(\boldsymbol{r})] = \sum_{k}^{nuclei} \int \frac{Z_k}{|\boldsymbol{r} - \boldsymbol{r}_k|}\rho(\boldsymbol{r}) d\boldsymbol{r} \tag{2.5}$$

While V_{en} is straightforward and can be found classically, the kinetic energy term T_e and the electron-electron potential V_{ee} are not so simple. Fortunately, Kohn and Sham thought to model these terms by making Hartree-Fock assumptions; they simplified the system to a non-interacting system of electrons. The energy equation from equation (2.3) is thus reconstructed as equation (2.6) below,

$$E[\rho(\boldsymbol{r})] = T_{ni}[\rho(\boldsymbol{r})] + V_{en}[\rho(\boldsymbol{r})] + V_{ee}[\rho(\boldsymbol{r})] + \Delta T[\rho(\boldsymbol{r})] + \Delta V_{ee}[\rho(\boldsymbol{r})] \tag{2.6}$$

where $T_{ni}[\rho(\boldsymbol{r})]$ is the kinetic energy of the non-interacting electrons, $\Delta T[\rho(\boldsymbol{r})]$ is the correction to the kinetic energy due to interactions between electrons, and $\Delta V_{ee}[\rho(\boldsymbol{r})]$ represents all non-classical corrections to the electron-electron repulsion potential. These corrections are summed up in the E_{xc} term, known as the exchange correlation energy.

From these equations, the electron density can be approximated and therefore also the energy of the system. The key difference between various methods or schools of thought lies with the exchange correlation energy, which corresponds to an error of less than 1 percent, however this is incredibly significant when working with Hartree-Focks (HF) as the unit of energy. In this study, the PBE0 (Perdew–Burke–Ernzerhof) hybrid exchange correlation is used, which is a member of the (hybrid) GGA (general-gradient-approximation) functionals family.

2.2.1. Numerical Details

The DFT geometry optimizations were carried out with ORCA version 6.0.1.[13–17] The PBE0 hybrid functional[18] was used, along with Grimme's D3 dispersion correction[19] with the Becke-Johnson damping scheme, D3BJ[20]. The basis set used for all atoms was def2-SVP[21], with the auxiliary basis def2/J[22]. Spin was treated using unrestricted Kohn-Sham (UKS), with 0 charge and a spin multiplicity of 1 for all complexes. A sample of the first five lines of the file is given below:

```
! UKS PBE0 D3BJ DEF2-SVP Opt Freq
!printbasis largeprint
 %pal nprocs 72 end
%maxcore 1500
* xyz 0 1
```

2.3. Workflow

To go from pincer ligands to magnesium complexes and their thermodynamic and geometrical quantities, a computational workflow was developed, based primarily on MACE and ORCA. To fill in the gaps and make the study high-throughput, a number of scripts were developed for file management, data extraction, and data analysis. The computation workflow is summarized by the flow chart in figure 2.1.

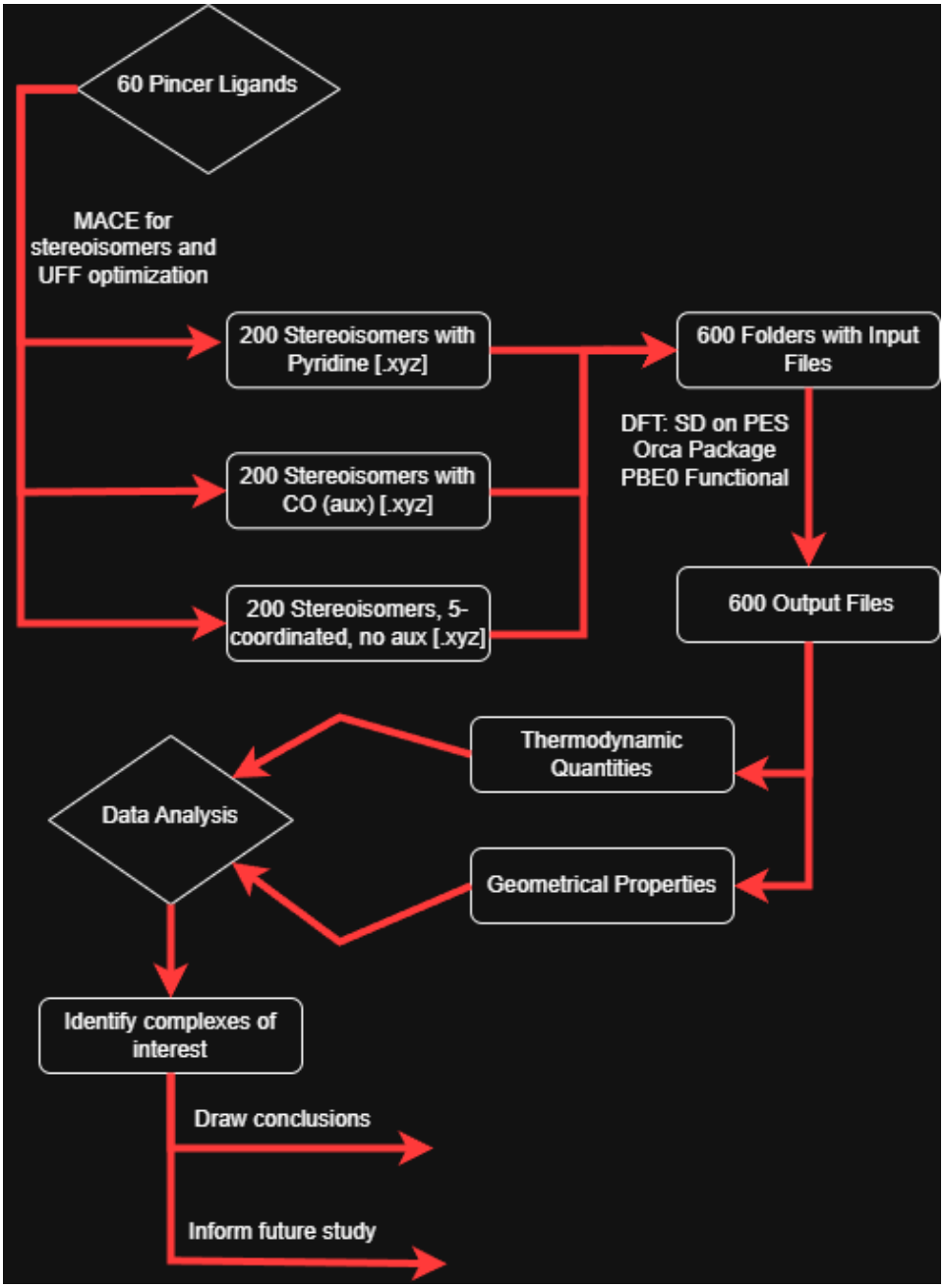

Figure 2.1: Computation workflow for this study

To begin, a list of pincer ligands and their SMILES was created by Olaf Koele as a Microsoft Excel sheet, which was then used in this study along with the studies of fellow students. This list of ligands was then imported into MACE, but since RDKit's sanitization checks did not accept the hypervalence of magnesium, ruthenium was instead used as a dummy atom. MACE was run for the excel sheet first with MgH_2L (5-coordinated), then for MgH_2COL where CO acts as an auxilliary ligand, and finally for MgH_2PxL, with pyridine coordinated. For each variation, 200 xyz files were generated, yielding a total of 600. An ensemble of bash and Python scripts were created for this study with the help of OpenAI's ChatGPT o3, o4-mini, and o4-mini-high models, allowing for vast automation. First, calculations were submitted onto the supercomputer DelftBlue, which yielded some initial key results, though due to compute time bottlenecks, this remained low-throughput. It was observed in these initial findings that CO is dispelled from the complex, and therefore does not coordinate. After this observation, the remaining CO calculations to be run were discarded to save on compute. To continue high-throughput, the files were instead run on the supercomputer Snellius. Once the calculations were complete, the ensemble of scripts was expanded to include data extraction. For thermodynamic data, the total thermal energies, Gibbs free energies, and enthalpies of all optimized complexes were extracted. For geometric data, the distance between the N-heteroatom in pyridine and the Mg central atom was calculated in addition to the pincer ligand asymmetry for the complexes with pyridine. This data was then analyzed and used to create the figures in the Results section using Python 3.13.3 and matplotlib 3.10.0.

3

Results & Discussion

Since the main purpose of this study is to find potential candidates for use in pyridine hydrogenation, it is useful to first look at the favorability of pyridine's coordination. To do so, structures were generated using MACE for each complex with pyridine coordinated, and with an empty site instead. The pincer ligands used for the subsequent results are shown in figure 3.1.

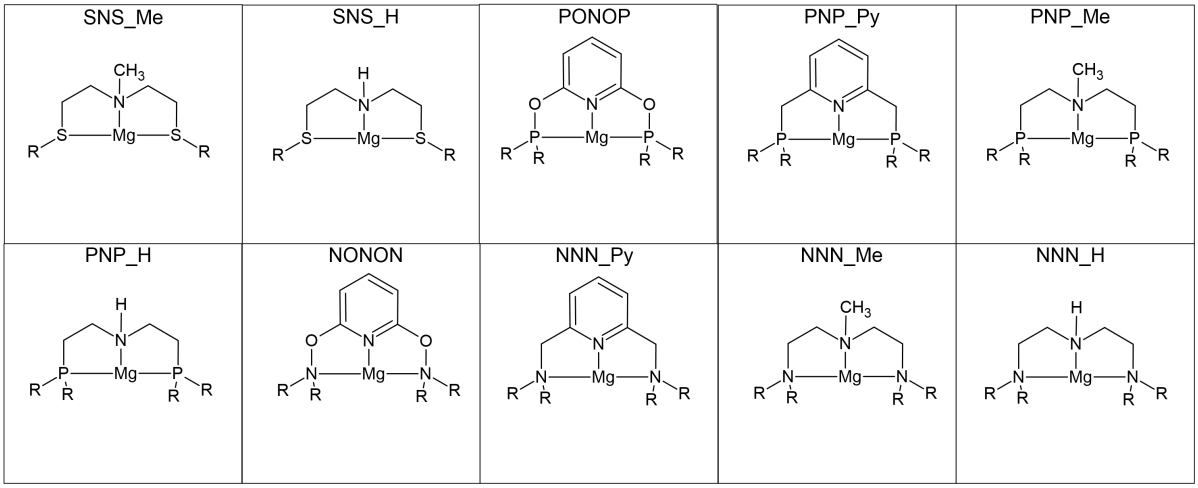

Figure 3.1: 2D Structures of the pincer ligands used, with either cyclohexane, methyl, phenyl, isopropyl, or tertbutyl as the R-groups, figure generated using ACD/Chemsketch

For each complex different conformers were generated, which can be divided into two groups. Some of the pincer ligands only adopt a meridional configuration, while the remaining pincer ligands can adopt both a meridional configuration and a facial configuration. For each configuration, there are two conformers, one where the donor atom of pyridine, or the empty site, is cis to the central donor atom of the pincer ligand, and one where it is trans. If the central donor atom of the pincer ligand for every complex is assigned the lower axial position, meaning that the remaining two donor atoms of each pincer ligand occupy equatorial sites, then the cis conformer is where the pyridine nitrogen is in the equatorial position, and the trans conformer is where the pyridine nitrogen is in the axial position. To illustrate this, two example pincer ligands are used from both of these groups. The two conformers for the ligands which only adopt a meridional configuration are shown in figure 3.2.

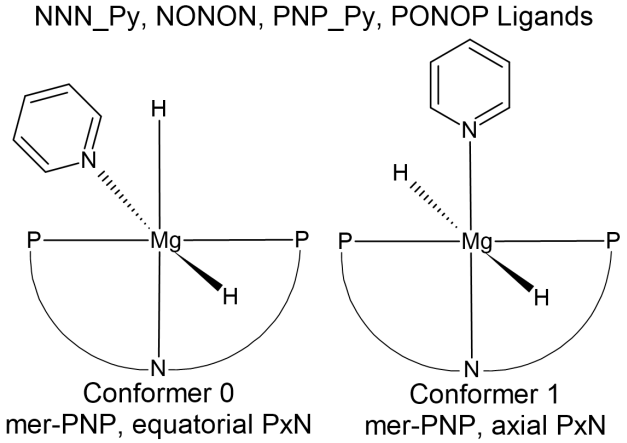

Figure 3.2: 2D structures of the two possible conformers of the PNP_Py pincer ligand, which can be generalized to NNN_Py, NONON, and PONOP pincer ligands in this study, figure generated using ACD/Chemsketch

For the ligands with both meridional and facial configurations, there are two possible conformers for each configuration, which are labelled as four total possible conformers, shown in figure 3.3.

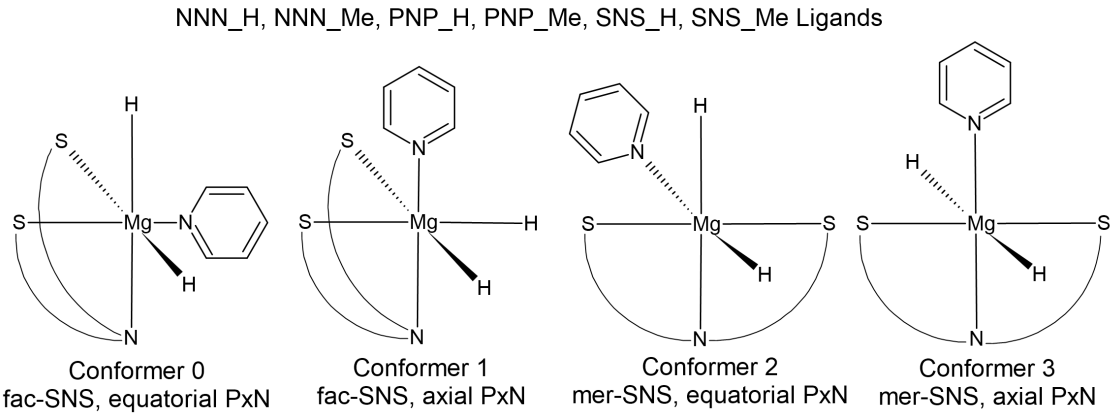

Figure 3.3: 2D structures of the two possible configurations of the SNS_Me pincer ligand, each with 2 possible conformers for a total of 4 conformers, which can be generalized to NNN_H, NNN_Me, PNP_H, PNP_Me, and SNS_H pincer ligands in this study, figure generated using ACD/Chemsketch

Conformer 0 and Conformer 2 in figure 3.3 match up to Conformer 0 of figure 3.2 in that the pyridine is equatorial, meanwhile Conformer 1 and Conformer 3 in figure 3.3 match up to Conformer 1 of figure 3.3 since pyridine is axial. However, confusingly, Conformer 0 and Conformer 1 in the two figures are not the same, because in figure 3.2 they are both the meridional configuration, whereas in figure 3.3, they are both the facial configuration. Instead, Conformer 2 and Conformer 3 in figure 3.3 are identical to Conformer 0 and Conformer 1, respectively, in figure 3.2.

3.1. Carbon Monoxide Auxiliary Ligand

Initially, the complexes were generated also using an auxiliary ligand, CO, at the same coordination site of pyridine or the empty site. However, after seeing an initial result, further calculations were abandoned to save on compute and time given the small scope of this study. The initial result is with the NONON pincer ligand, shown below in figure 3.4.

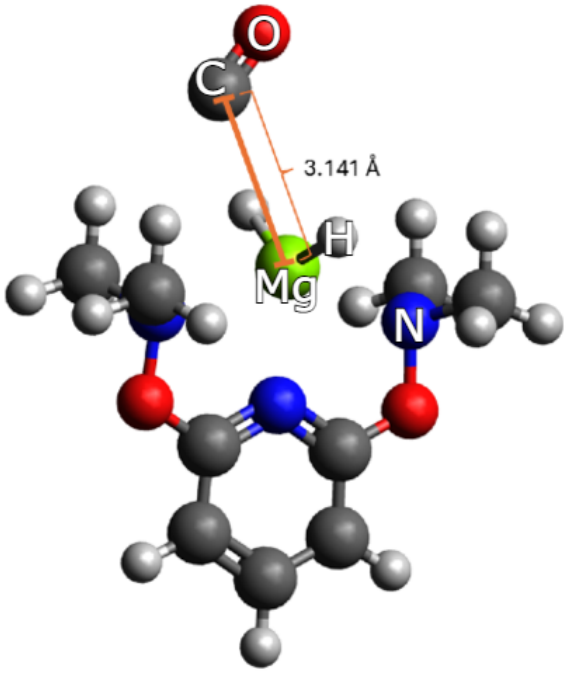

Figure 3.4: 3D Structure of the NONON pincer ligand with methyl R-groups, Conformer 1, showing the expulsion of the CO auxiliary ligand from its coordination position, 3D visualization created using Avogadro

As can be seen in figure 3.4, the complex assumes a 5-coordinated environment, preferring to kick out the auxiliary ligand rather than keep it coordinated. While CO does not help to stabilize the complex in this case, since this study does not investigate CO further as an auxiliary ligand, it is possible that some complexes would indeed allow CO to coordinate and potentially be thereby stabilized.

3.2. Energetics

The centerpiece of this study is the favorability of pyridine's coordination to the various studied complexes. Both for readability and to help narrow down, Figure 3.5 shows only the most stable conformer found for each combination of pincer ligand and R-group, and these same complexes are shown in all subsequent plots. The full energy data for all conformers can be found in the Appendix in figure A.1.

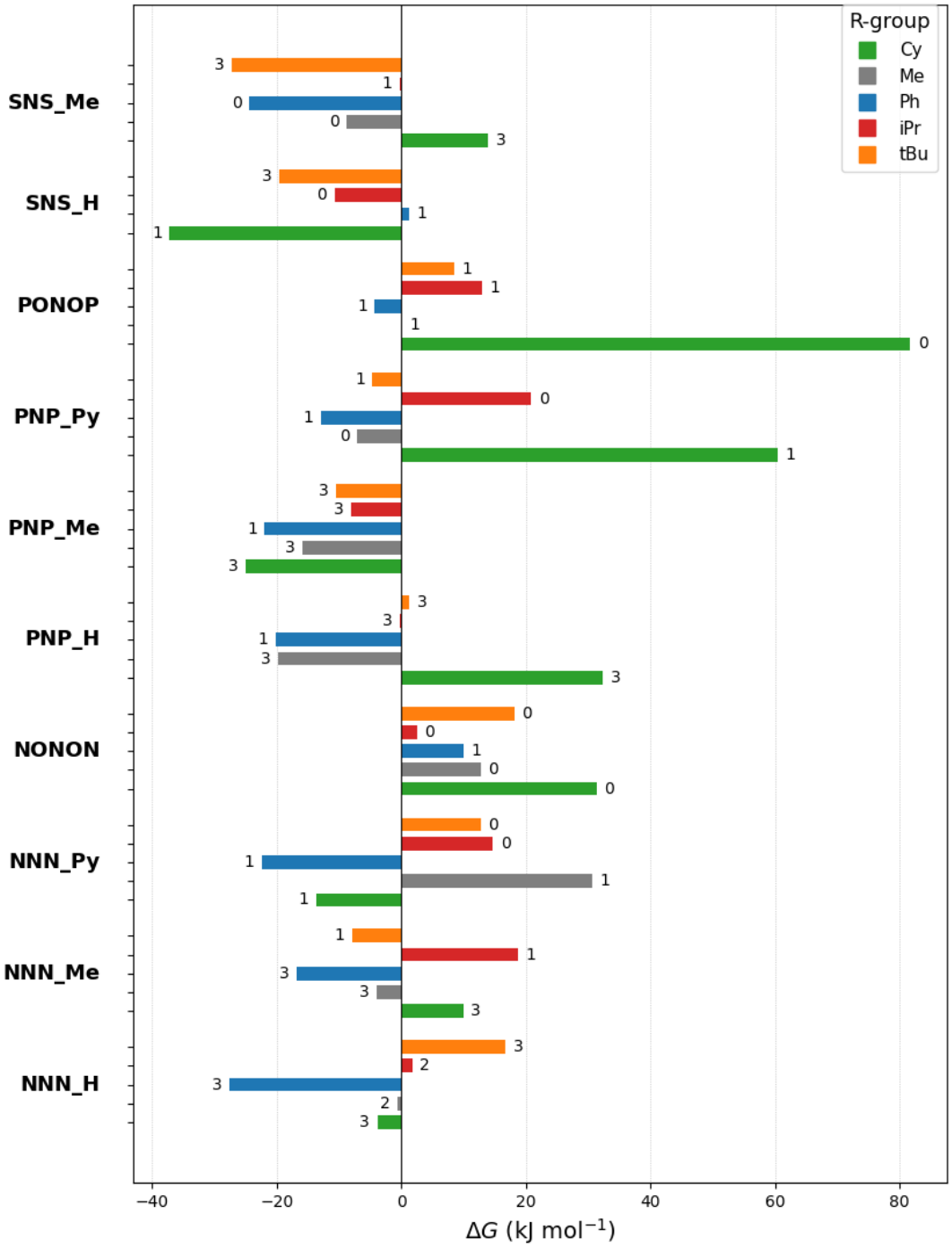

Figure 3.5: Gibbs free energies of the most stable conformer for each combination of pincer ligand and R-group with pyridine conformer, using the most stable conformer before pyridine coordination as reference

As seen above in figure 3.5, SNS, NNN, and PNP-type ligands appear most stable with pyridine coordination. There is diversity in the favorability of the R-groups, however, phenyl groups seem most stabilizing on average. Quite a number of complexes favor the coordination of pyridine, suggesting that magnesium has the potential to catalyze pyridine reactions.

The next plot, figure 3.6, shows the distance in angstrom between the nitrogen in the coordinated pyridine and the magnesium of each complex. There is a notable split in the plot, with the majority of data falling below 2.5 angstrom, suggesting coordination, and then a smaller group of points for the NONON and NNN_H ligands falling above 4.0 angstrom, indicating that pyridine does not coordinate.

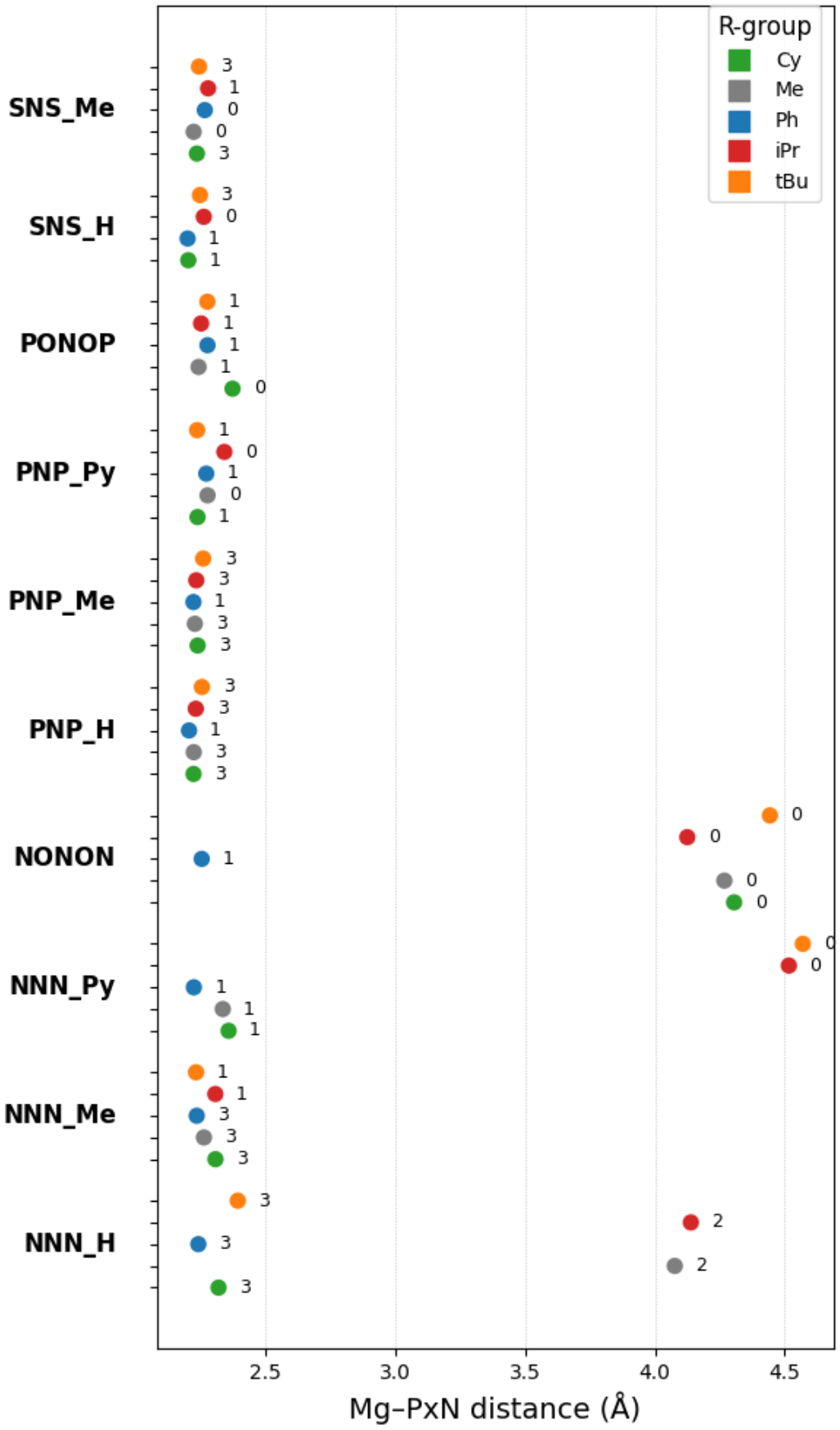

Figure 3.6: Distance between the magnesium and nitrogen atom in the coordinated pyridine for the most stable conformer complexes

To obtain a better indication of the favorable complexes' viability in practice, energies were also obtained for the coordination of 3 additional pyridines after the coordination of the first pyridine. The favorability of this process is not desired, as it indicates instability of the complex in the presence of pyridine.

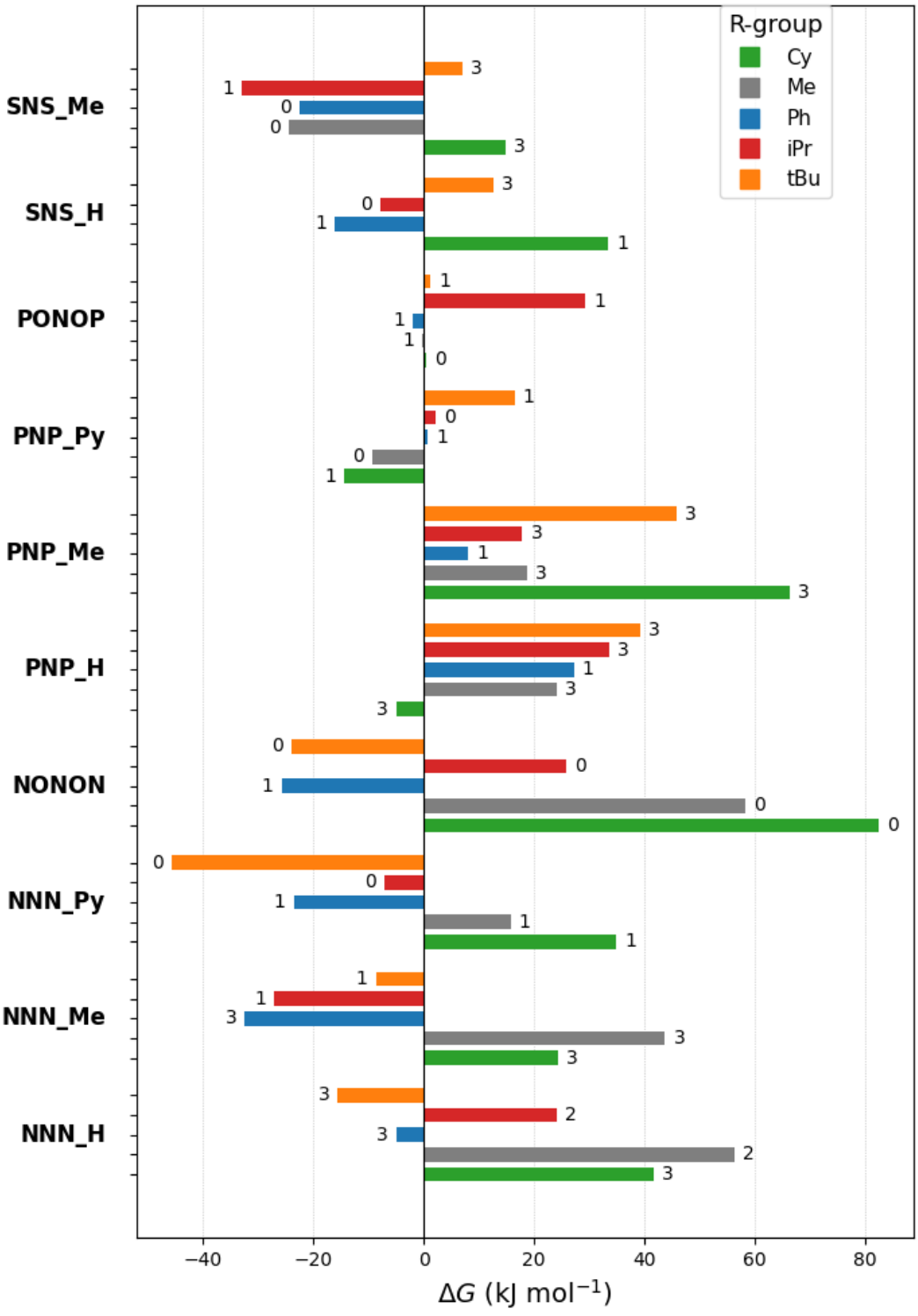

Figure 3.7: Energy for the full dissociation of the pincer ligand, going from one pyridine coordinated as the reference to four pyridines coordinated

The next plot combines data from figure 3.5 and figure 3.7, showing only the complexes which simultaneously favor the coordination of one pyridine, but do not favor the coordination of three additional pyridine molecules.

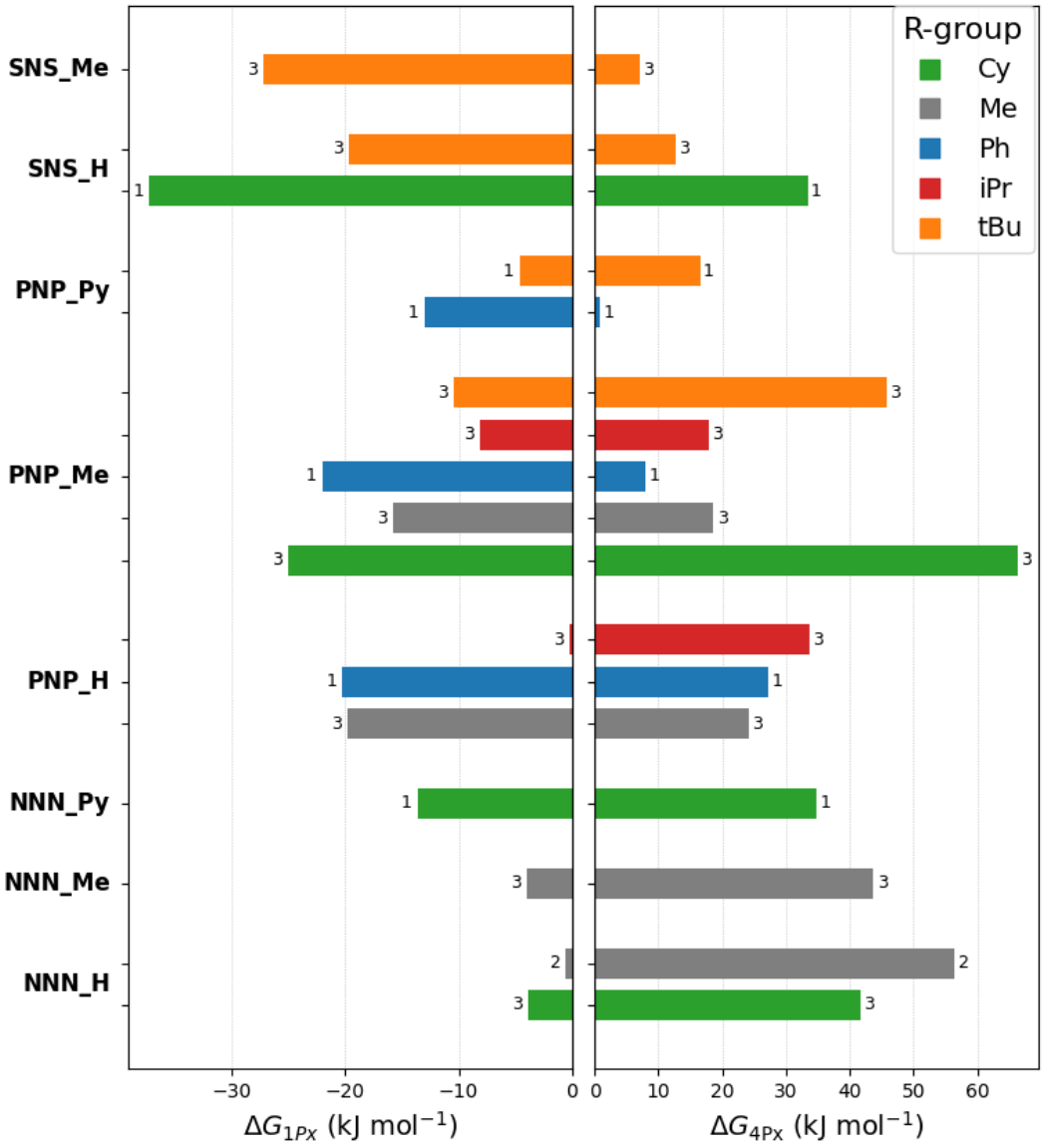

Figure 3.8: Combined graph of the change in Gibbs free energy of 1 pyridine associating (left) and 4 pyridines associating to kick out ligand (right)

From figure 3.8, it is evident that the ligand screening has yielded a number of magnesium pincer ligand complexes which are potential candidates for pyridine hydrogenation. While the study is high-throughput, it is now useful post-screening to use a low-throughput approach by looking at the individual structures. While all of the complexes shown in figure 3.8 may yield interesting insights, the structures of the most stable complexes will be the focus, while still aiming for a diverse selection.

First, the complex for which the coordination of the first pyridine is most favored in figure 3.8, the SNS_H with cyclohexane as the R-group. The structure of this complex is shown in figure 3.9.

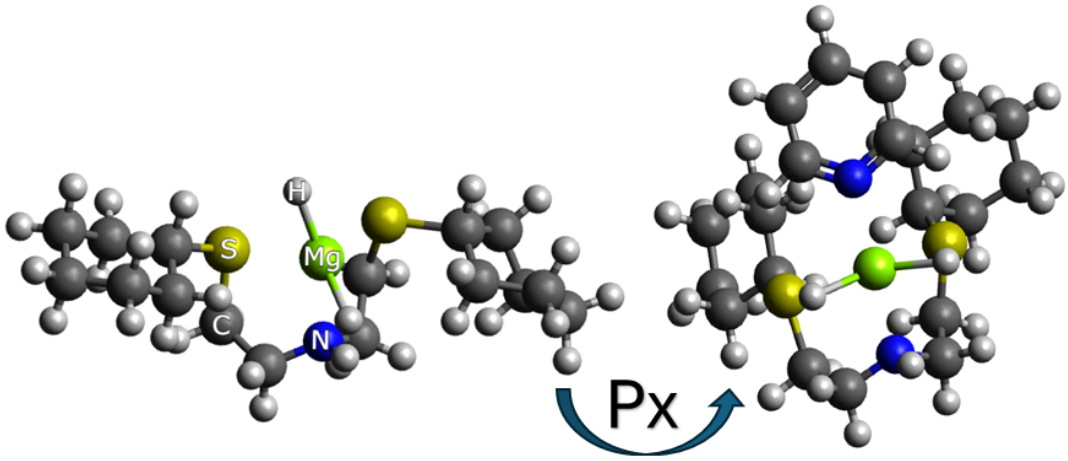

Figure 3.9: MgH_2 Complex with coordinated SNS_H Ligand with cyclohexane R-groups, Conformer 1, 3D visualization created using Avogadro

Second, the complex with the third most favorable coordination of the first pyridine, and least favourable association of the additional three pyridines, the PNP_Me complex, also with a cyclohexane R-group is shown in figure 3.10.

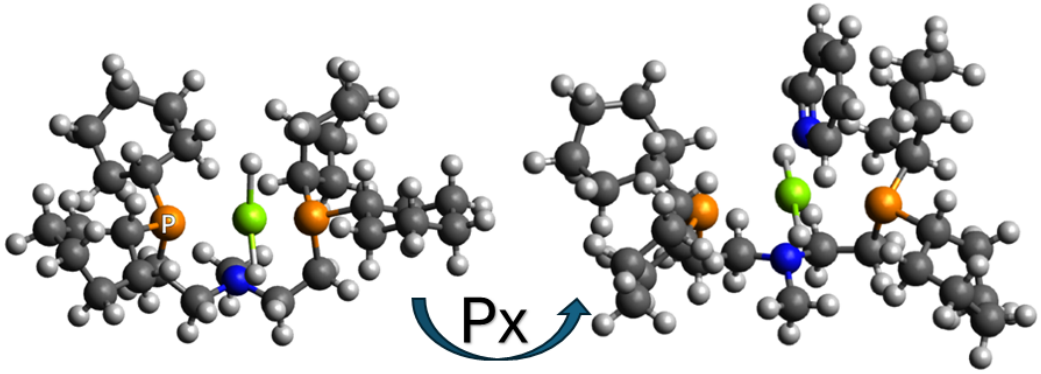

Figure 3.10: MgH_2 Complex with coordinated PNP_Me Ligand with cyclohexane R-groups, Conformer 3, 3D visualization created using Avogadro

The third complex displayed low-throughput is PNP_H ligand with phenyl R-groups, as this is the next most stable ligand regarding the association of the first pyridine which appears stable with respect to the full replacement of the ligand with pyridines, shown in figure 3.11.

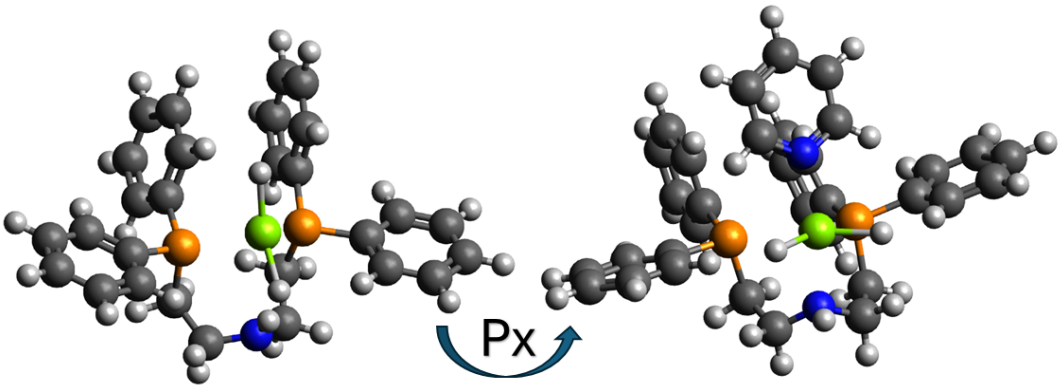

Figure 3.11: MgH_2 Complex with coordinated PNP_H Ligand with phenyl R-groups, Conformer 1, 3D visualization created using Avogadro

The complex without pyridine shows a surprising result, which is that it favors a 4-coordinated environment over a 5-coordinated environment, and to accomplish this, displays N-hemilability in the PNP ligand. Once pyridine is introduced, however, the N in the pincer does indeed coordinate, forming a 6-coordinated complex.

The final complex shown is the PNP_H ligand with methyl R-groups, having the same ligand as the prior, and showing similar energetics, in addition to being a possible candidate in its own right. It is depicted in figure 3.12 below.

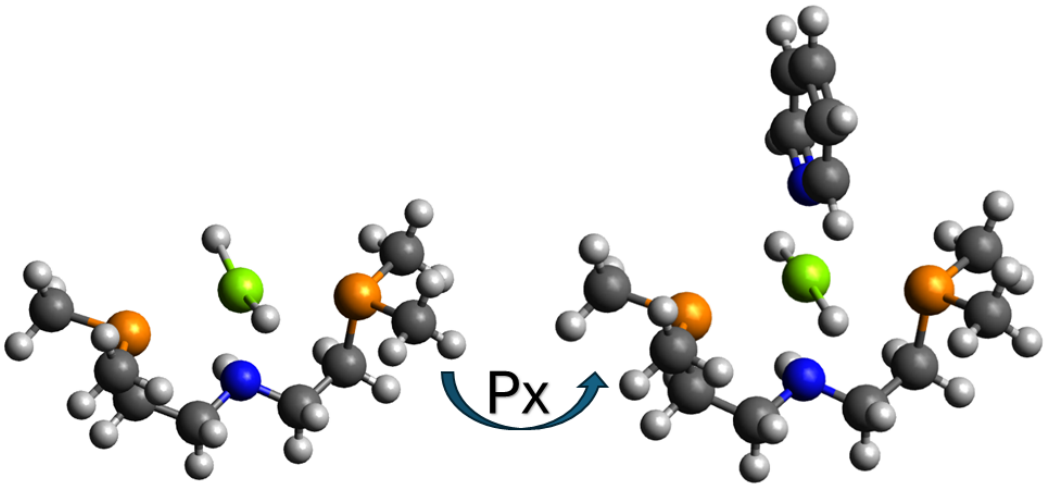

Figure 3.12: MgH_2 Complex with coordinated PNP_H Ligand with methyl R-groups, Conformer 3, 3D visualization created using Avogadro

3.3. Hemilability

In addition to the energetics, it is also intriguing to investigate whether the complexes in this study demonstrate hemilability. One example of hemilability is already identified coincidentally in the low-throughput analysis of figure 3.11, but a high-throughput investigation is also desirable. For simplicity, potential hemilability is identified by calculating the difference between the furthest donor atom to the metal center and the second furthest atom to the metal center, and then checking whether this surpasses a given threshold. The results of this hemilability check are shown in the following figure, figure 3.13.

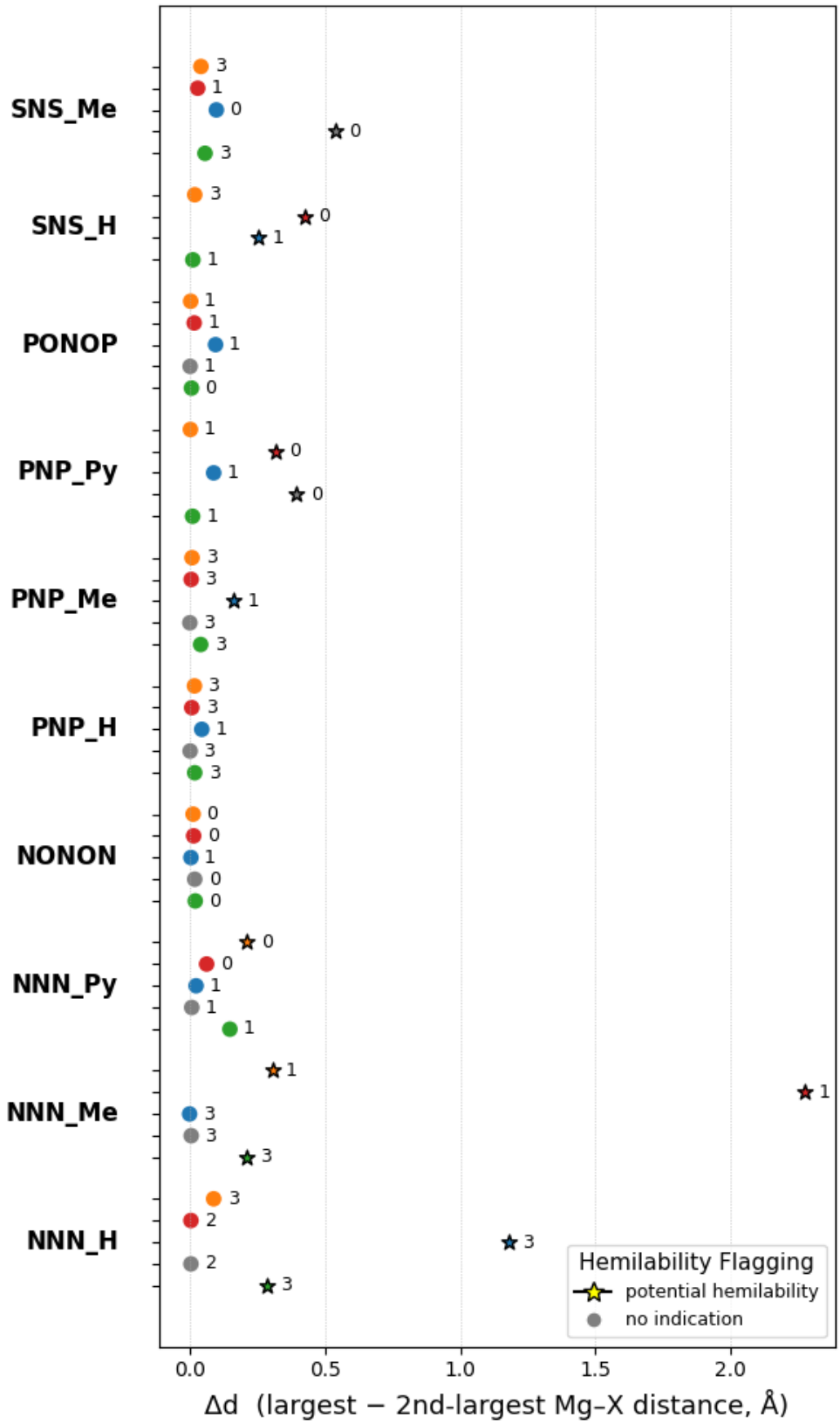

Figure 3.13: Difference in the distances between the furthest and second furthest donor atom from the central magnesium atom. Hemilability flagged for asymmetric pincer ligands above certain thresholds.

In figure 3.13, there are a number of complexes marked as potentially hemilabile, however NNN_Me with the isopropyl R-groups and NNN_H with the phenyl R-groups stand out in the degree of asymmetry found. Additionally, PNP_Me with phenyl R-groups and NNN_H with cyclohexane R-groups are flagged for hemilability, and are also shown as potential candidates in figure 3.8.

Starting with the greatest difference in distances, the NNN_Me with isopropyl R-groups is shown, both before and after pyridine coordination, in figure 3.14 below.

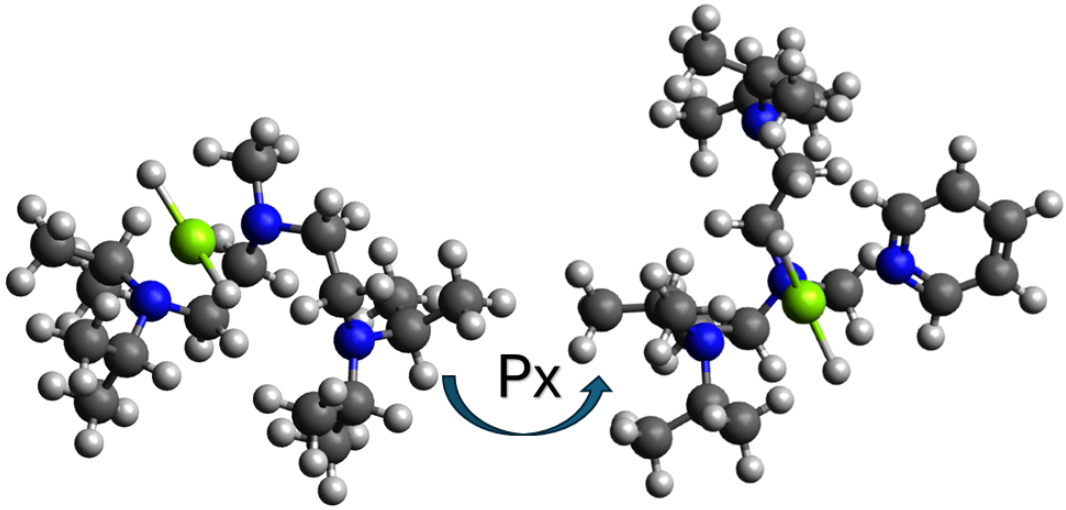

Figure 3.14: MgH_2 Complex with coordinated NNN_Me Ligand with isopropyl R-groups, Conformer 1, 3D visualization created using Avogadro

Interestingly, figure 3.14 matches the result found in figure 3.11, in that the hemilability is already present before the coordination of pyridine, and the complex assumes a 4-coordinated environment, perhaps to sterically accommodate the bulky R-groups in both cases. However, in this case, the ligand arm remains dissociated after coordination of pyridine, assuming a 5-coordinated environment, as seen in the right of figure 3.14.

Moving onto the next ligand, the structure of the NNN_H complex with phenyl R-groups is shown in figure 3.15 below.

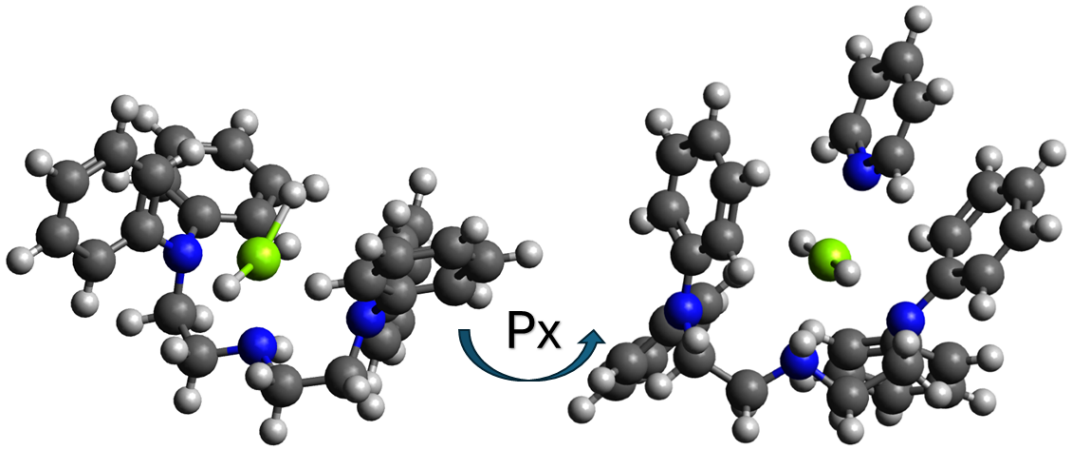

Figure 3.15: MgH_2 Complex with coordinated NNN_H Ligand with phenyl R-groups, Conformer 3, 3D visualization created using Avogadro

On the left side of figure 3.15, the complex does display some asymmetry, however it does not appear to display hemilability as it still has a 5-coordinated geometry. After adding pyridine, however, the

asymmetry increases significantly, but the ligand arm does not appear to fully dissociate. It looks as if the complex is somewhere in between a 6-coordinated and 5-coordinated environment.

Next, the structures of the two potentially hemilabile complexes which are also candidates will be investigated, starting with that of PNP_Me with phenyl R-groups in figure 3.16 below.

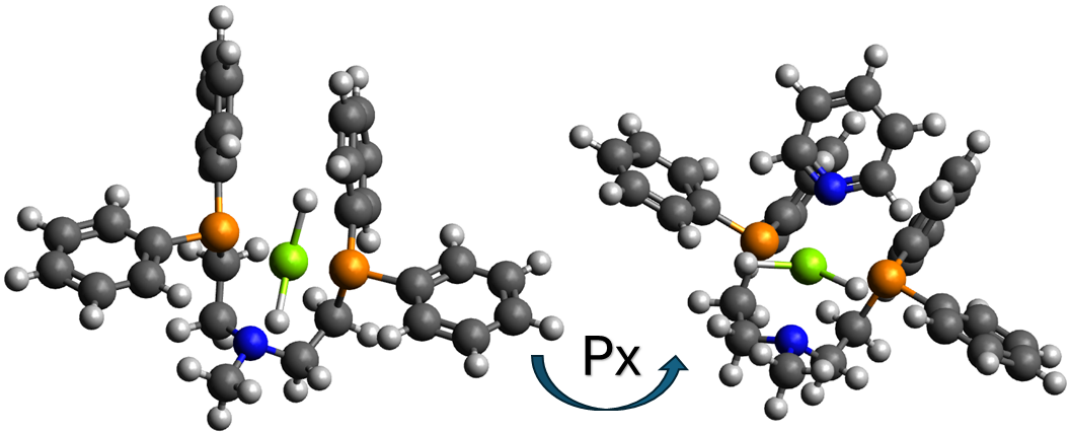

Figure 3.16: MgH_2 Complex with coordinated PNP_Me Ligand with phenyl R-groups, Conformer 1, 3D visualization created using Avogadro

While the complex in figure 3.15 is flagged for potential hemilability, the ligand does not appear to actually show hemilability, as the formed complex on the right side still has a roughly octahedral geometry. There is indeed some asymmetry between the two phosphorous donor atoms, but it does not appear to be pronounced enough to indicate true hemilability of the ligand. The same is observed in the structure of the other candidate structure marked as potentially hemilabile, the NNN_H with cyclohexane R-groups, so the structure will be not be shown here. The candidates found for pyridine hydrogenation appear to largely not demonstrate hemilability.

4

Conclusion & Outlook

This study on using magnesium pincer complexes to catalyze the hydrogenation of pyridine determines the stability of 137 different magnesium-based pincer complexes. The energies of the complexes without pyridine, with a single pyridine coordinated, and with four pyridines coordinated to kick out the pincer ligand are calculated. The distance between the nitrogen in pyridine and the magnesium central atom is found for each complex to determine coordination. Hemilability of the complexes with one pyridine coordinated is predicted based on the asymmetry of the pincer ligand, calculated by the difference in distances to the metal center. A total of 17 potential complexes are found as candidates, with a smaller selection of 4 complexes found to be particularly stable. The structures of these complexes are elucidated, giving insight into their geometries. The structures of select complexes flagged as hemilabile are shown.

The results of this study provide a strong basis for furthering the growing literature on main-metal catalysis. Specifically, the successes of Liang et al. in using PNP, PNN, and NNN magnesium pincer complexes for the hydrogenation of alkenes and semihydrogenation of internal alkynes can be expanded to pyridine, and to a more diverse set of pincer ligands.[8] A handful of stable magnesium pincer complexes are found to potentially catalyze the hydrogenation of pyridine. Additionally, some insights into the geometries and notably the hemilability of these complexes are generated by this study.

The findings of this study are limited in scope due to certain technical faults and the small scope compared to previous studies. Firstly, the optimization of a number of complexes did not converge, notably all of the PNN ligands, due to a mistake in the generation of their initial geometries. However, more importantly, this study is limited in that it investigates only the coordination of pyridine and the stability of the formed complex, including the risk of the pincer ligand dissociating in the presence of pyridine. It is therefore difficult to draw broader conclusions in the order of magnitude of Liang et al. or Sharma et al.'s studies about the overall hydrogenation pathway.[8,9] The mechanistics of the reaction are also not investigated by this study. What this study does provide is a solid foundation for further research into the possibilities of magnesium pincer complexes, specifically by screening a wide array of initial candidates to find much more promising candidates that can be further investigated low-throughput in greater detail.

Future research could use these candidates for the aim of developing viable main-metal catalysts for the hydrogenation of N-heterocycles. The four complexes selected as the most viable, SNS_H with cyclohexane R-groups, PNP_Me with cyclohexane R-groups, PNP_H with phenyl R-groups, and PNP_H with methyl R-groups could be synthesized to determine whether they are are stable under real conditions. If the complexes are stable, then the hydrogenation of pyridine could be studied directly by performing the full catalytic cycle. The final aim would be to more broadly apply these complexes to the hydrogenation of N-heterocycles, as this would provide a main-metal alternative to current catalysts.

References

[1] Zhang, Y.; Wang, J.; Zhou, F.; Liu, J. *Catal. Sci. Technol.* **2021**, *11*, 3990–4007.

[2] Gianotti, E.; Taillades-Jacquin, M.; Rozière, J.; Jones, D. J. *ACS Catalysis* **2018**, *8*, 4660–4680.

[3] Shimbayashi, T.; Fujita, K.-i. *Tetrahedron* **2020**, *76*, 130946.

[4] Peris, E.; Crabtree, R. H. *Chem. Soc. Rev.* **2018**, *47*, 1959–1968.

[5] Sánchez, P.; Hernández-Juárez, M.; Rendón, N.; López-Serrano, J.; Santos, L. L.; Álvarez, E.; Paneque, M.; Suárez, A. *Dalton Trans.* **2020**, *49*, 9583–9587.

[6] Rauch, M.; Kar, S.; Kumar, A.; Avram, L.; Shimon, L. J. W.; Milstein, D. *Journal of the American Chemical Society* **2020**, *142*, PMID: 32786799, 14513–14521.

[7] Kar, S.; Milstein, D. *Chem. Commun.* **2022**, *58*, 3731–3746.

[8] Liang, Y.; Das, U. K.; Luo, J.; Diskin-Posner, Y.; Avram, L.; Milstein, D. *Journal of the American Chemical Society* **2022**, *144*, PMID: 36194894, 19115–19126.

[9] Sharma, V.; Dash, S. R.; Vanka, K.; Gonnade, R. G.; Sen, S. S. *Organometallics* **2025**, *44*, 875–881.

[10] Chernyshov, I. Y.; Pidko, E. A. *Journal of Chemical Theory and Computation* **2024**, *20*, PMID: 38365199, 2313–2320.

[11] Sylvia, R. Interstitial Oxygen Defects in β-Si3N4, Unpublished manuscript for LO2 Project, Department of Theoretical Chemistry, University of Leiden, 2024.

[12] Cramer, C. J., *Essentials of Computational Chemistry*; Wiley: 2004.

[13] Neese, F. *WIREs Computational Molecular Science* **2022**, *12*, e1606.

[14] Neese, F.; Wennmohs, F.; Hansen, A.; Becker, U. *Chemical Physics* **2009**, *356*, Moving Frontiers in Quantum Chemistry: 98–109.

[15] Bykov, D.; Petrenko, T.; Izsák, R.; Kossmann, S.; Becker, U.; Valeev, E.; Neese, F. *Molecular Physics* **2015**, *113*, 1961–1977.

[16] Helmich-Paris, B.; de Souza, B.; Neese, F.; Izsák, R. *The Journal of Chemical Physics* **2021**, *155*, 104109.

[17] Neese, F. *Journal of Computational Chemistry* **2023**, *44*, 381–396.

[18] Adamo, C.; Barone, V. *J. Chem. Phys.* **1999**, *110*, 6158–6170.

[19] Grimme, S.; Antony, J.; Ehrlich, S.; Krieg, H. *The Journal of Chemical Physics* **2010**, *132*, 154104.

[20] Grimme, S.; Ehrlich, S.; Goerigk, L. *Journal of Computational Chemistry* **2011**, *32*, 1456–1465.

[21] Weigend, F.; Ahlrichs, R. *Phys. Chem. Chem. Phys.* **2005**, *7*, 3297–3305.

[22] Weigend, F. *Phys. Chem. Chem. Phys.* **2006**, *8*, 1057–1065.

A

Appendix

AI Use Declaration

None of the text or images in this report are direct outputs of large-language models or other AI-tools. However, ChatGPT by OpenAI is used extensively in this study both for consultation and for the generation of python and bash scripts, specifically the o3, o4-mini, and o4-mini-high models. These scripts are used extensively for automation throughout the study and also to create the plots used in this report.

The full energy plot of all conformers is shown in figure A.1 below.

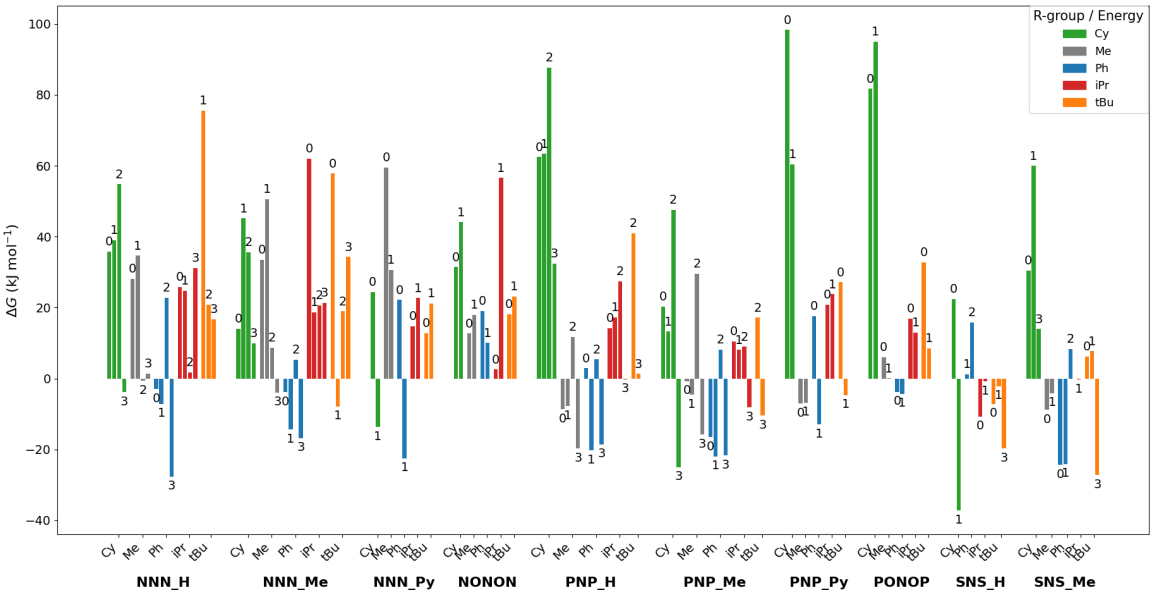

Figure A.1: Gibbs free energies of all conformers using the most stable conformer before pyridine coordination as reference, expanded version of figure 3.5)